Correlative spectroscopy of silicates in mineralised nodules formed from osteoblasts

Suwimon Boonrungsiman[a,b], Sarah Fearn[a], Eileen Gentleman[a,c], Liam Spillane[a], Raffaella Carzaniga[a,d], David W. McComb[a,e], Molly M. Stevens[a,f,*] Alexandra E. Porter[a*]

Silicon supplementation has been shown to play an important role in skeleton development, however, the potential role that silicon plays in mediating bone formation, and an understanding of where it might localise in the resulting bone tissue remain elusive. An improved understanding of these processes could have important implications for treating pathological mineralisation. A key aspect of defining the role of silicon in bone is to characterise its distribution and coordination environment, however, there is currently almost no information available on either. We have combined a sample-preparation method that simultaneously preserved mineral, ions, and the extracellular matrix (ECM) with secondary ion mass spectroscopy (SIMS) and electron energy-loss spectroscopy (EELS) to examine the distribution and coordination environment of silicon in *murine* osteoblasts (OBs) in an *in vitro* model of bone formation. SIMS analysis showed a high level of surface contamination from polydimethysiloxane (PDMS) resulting from sample preparation. When the PDMS was removed, silicon compounds could not be detected within the nodules either by SIMS or by energy dispersive x-ray spectroscopy (EDX) analysis. In comparison, electron energy-loss spectroscopy (EELS) provided a powerful and potentially widely applicable means to define the coordination environment and localisation of silicon mineralising tissues. We show that trace levels of silicon were only detectable from the mineral deposits of the mineralised nodules. Taken together our results suggest that silicon plays a biological role in bone formation, however, the mechanism by which silicon exerts its physicochemical effects remains uncertain. Our analytical results open the door for compelling new sets of EELS experiments that can provide detailed and specific information about the role that silicates play in bone formation and disease.

1. Introduction

Several reports have indicated that silicon plays an important role in bone formation by increasing matrix synthesis and the differentiation of osteoblast cells[1-6]. Silicon has also been found to be essential for skeleton development[1-4], and chickens fed with a Si-deficient diet have significantly smaller, shorter and thinner leg bones[3] compared to chickens treated with a silicon supplemented diet. Si-deficiency also causes abnormalities in the skulls of rats; they are distorted and shorter than in normal healthy rats[2]. Addition of silicon compounds to osteoblast cell cultures has also been reported to have a biochemical effect on osteoblast function and appears to play a role in mineralization[5, 6]. Silicon has been shown to be an essential element in the synthesis and formation of collagen[2-5] and *in vitro* studies demonstrated positive effects of silicon on osteoblast proliferation and activity[5]. The silicon containing compound, zeolite A (ZA), which is composed of $(SiO_4)^{4-}$ and $(AlO_4)^{5-}$, promoted DNA synthesis, alkaline phosphatase (ALP) activity, osteocalcin production and a post-translational process of transformation growth factor (TGF-β) in osteoblasts (OB)[5]. It is also widely accepted that incorporation of 0.8wt% silicon into calcium phosphate increases the bioactivity of implants[6-8]. Silicon susbstituted hydroxayaptite (Si-HA) implants were able to promote bone remodelling around the implant, as evidenced by the collagen fibrils being more aligned and organized around the Si-HA implant 6 weeks after implantation[8]. Si-HA also increased the alkaline phosphatase (ALP) activity and total protein production by human OBs in culture compared to pure HA[6]. In short, silicon appears to affect osteoblast function and bone formation, however, the localisation and coordination environment of silicon within bone tissue (*i.e.* whether it partitions to the collagen fibrils, mineral or cells) remain elusive.

Despite the interest in the role of silicon in bone formation and mineralisation, there is almost no information available about the distribution of silicon in bone. Furthermore, no studies are available which have characterised the coordination environment of the silicon due to the complexity of performing this analysis. In a series of experiments using electron probe microanalysis, Carlisle reported detection of silicon (up to a maximum level of 0.5 wt %) within the unmineralized osteoid regions, that is, active calcification sites, of normal tibiae from young mice and rats[4]. A later report by Landis *et al.*, mapped the distribution of silicon and calcium in the growing long bones which had been prepared using anhydrous organic solvents from normal embryonic chicks and young rats by SIMS[1]. This work supported the earlier work by Carlisle and showed that silicon localised to the putative uncalcified osteoid regions of tibiae [(1)]. However neither study thoroughly examined the preparation protocol relative to silicon or provided information about the coordination environment of the silicon; the room temperature preparation methods used may lead to movement, redistribution or loss of silicon during tissue processing. In addition, it is not clear from these earlier studies whether any silicon contamination had been removed. Despite the remarkable developments that have occurred in the field of nanometer-scale analysis over the past decade, no nanoscale analytical studies have followed up on these early studies.

One of the major challenges with mapping the distribution of silicon in tissues arises due to the low levels present, typically only 100 ppm is present in bone and ligament[2]. Very few techniques are

therefore available to detect the low concentrations of silicon present. Preservation of the native structure and chemistry of the tissue is also challenging and artefacts introduced during TEM sample preparation can be extremely subtle. It is also challenging to remove silicon-containing contaminants from the surface of the sample which can be problematic since these contaminants interfere with subsequent STEM-EELS analysis of both silicon and also phosphorus. The aim of this study is to map the distribution of silicon in mineralised bone tissue nodules formed from OBs. The combination of time of flight (TOF)-SIMS with spatially resolved nanoanalytical electron microscopy techniques could be advantageous for identifying the source of contamination. OBs are bone forming cells *in vivo* and form mineralised nodules *in vitro* when cultured under specific conditions. Our previous studies have demonstrated that they act a good model to study bone mineralisation[9, 10]. Through this study, we aim to develop a protocol which allows for simultaneous preservation and detection of the chemistry and structure of ions, minerals and cell ultrastructure within the bone mineralised nodules, to accurately map the distribution of elements and their coordination environment during the early stages of bone formation.

2. Materials and Methods

2.1 Silicon-substituted hydroxyapatite (Si-HA) with 0.8 wt. % silicate ion substitution was produced the aqueous precipitation reaction between calcium hydroxide [$Ca(OH)_2$] and orthophosphoric acid [$H_3(PO)_4$] with silicon acetate [$Si(CH_3COO)_4$] as the silicon source[11]. The resulting compound was mixed with a low molecular weight polymer to form a slip, which is then agitated to create a foam. Once dry, the material was sintered at 1250 °C to burn out the polymer and densify the ceramic. The resulting material has interconnected total porosity of 80 % ± 2.5%. Details of the characterization of the porous Si-HA granules (X-ray diffraction, level of porosity) are given elsewhere[12].

2.2 Primary cell extraction

Mouse calvarial osteoblasts (OBs) were isolated, expanded and cultured to form mineralised nodules according to the protocols described previously[9]. Briefly, mouse OBs were obtained from calvarias of neonatal mice (2 days old). Calvarias were removed, washed in phosphate buffered saline, cut and then digested 5 times in a 10% v/v solution of 0.05% v/v trypsin/EDTA (Invitrogen) in Hank's balanced salt solution containing 1.0 mg/mL collagenase at 37°C, 20 minutes for each of the first 4 digestions and 2 hours for the last digestion. Supernatant from the last 3 digestions was pooled and centrifuged at 200g for 5 minutes to collect cell pellets. The cell pellet was re-suspended in αMEM supplemented with 15% v/v FBS and 1X P/S and plated on standard tissue culture plastic.

2.3 Mineralised nodule formation

To induce mineralized nodule formation, cells were plated on sapphire discs (Leica Microsystems) at 30,000 cells/cm^2 in αMEM supplemented with 15% (v/v) FBS, 1X P/S, 50 µg/mL ascorbic acid, and 10 mM β-glycerophosphate (both from Sigma) according to a widely use protocol for *in vitro* differentiation of mineralising cells [13-21]. Dexamethasone was added to all cultures at a concentration of 1 µM beginning at day 14 and cultivation was continued until day 28. The culture medium was changed every two days.

2.4 Sample preparation for TEM

Mineralised nodules (on sapphire disc) were placed on specimen carriers with 200 µm deep cavities, mounted in a 20% (w/v) solution of bovine serum albumin (Sigma) in αMEM and frozen using with a Leica EM PACT 2 high pressure freezer. Freeze-substitution was performed in a Leica EM AFS2 freeze substitution device using an anhydrous solution of acetone containing a 3% (v/v) glutaldehyde, 1% (w/v) osmium tetroxide and 0.5% (w/v) uranyl acetate at -90 ˚C for 8 hours. Samples were then gradually warmed to 0 ˚C at 5 ˚C/hour, washed twice in acetone, brought to room temperature and infiltrated with Quetol-based resin (12.6g Quetol, 15.5g Nonenyl succinic anhydride (NSA), 6.5g Methyl nadic anhydride (MNA) and 0.6g Benzyl dimethylamine (BDMA)). The specimens were infiltrated in the Quetol-based resin at a ratio of 1:1, 3:1 (resin: acetonitrile) and pure resin for 2 hours, overnight and 4 days, respectively. Pure resin was changed every 24 hours. Embedded samples were polymerized at 60˚C for 24 hours. 70 nm thick sections were cut onto a water bath *via* ultramicrotomy using a 35º diamond knife. The sections were collected immediately on bare 300 mesh copper TEM grids and dried immediately on filter paper. Particular care was given to preserve the chemistry of the mineral and also to reduce any contamination. The EELS study was carried out in 5 different regions within the OB nodule. A full discussion of the sample preparation protocols used is provided in ref.10.

2.5 Scanning transmission electron microscopy (STEM)

High angle annular dark field STEM (HAADF-STEM) and STEM-EELS were performed on a Titan 80/300 STEM/TEM operated at 300kV. STEM images were recorded using a HAADF detector with inner and outer semi-angle of 40 and 196 mrad, respectively. EELS was carried out in STEM mode under the same operating conditions. The convergence and collection semi-angles into the spectrometer were set to 6.8 and 8.90 mrad, respectively. The energy resolution was 1 eV and the dispersion was set to 0.1 eV/pixel to collect the characteristic Si $L_{2,3}$- edge. The EEL spectra were acquired from an area that had a relative thickness (t/λ) of less than 0.4. A more detailed description of the STEM-EELS protocols can be found in ref. 10 .

2.6 STEM-EDX

The EDX spectra were collected using a Tecnai F20XT microscope operating at 200kV. In STEM mode the sample was tilted to face the EDAX SiLi EDX detector to optimise the signal.

2.7 Time of flight secondary ion mass spectrometry (TOF-SIMS)

ToF-SIMS was carried out using an Ion Tof ToF-SIMS V instrument. The instrument is fitted with a 25 keV Bi^+ analytical ion beam and Cs^+, O_2^+ and C_{60}^+ sputter ion beams. The SIMS instrument was used to obtain both ion images and mass spectra from the sample. In both the imaging and mass spectra modes positive secondary ions were collected. The electron flood gun (20eV) was also applied to avoid charging of the sample during the

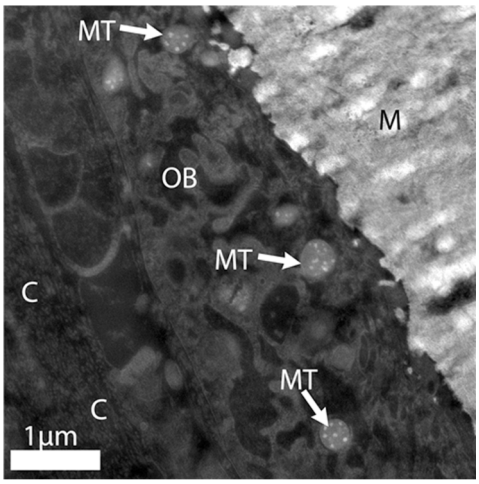

Figure 1: HAADF-STEM image of a cross section through osteoblast (OB) nodules showing the OBs surrounded by a collagenous matrix (C) and mineralized collagen (M). Mitochondria (Mt) containing calcium phosphate are present within the OBs (arrows).

analyses.

2.8 Ion- imaging

The sputter cleaning was performed using the 10keV C_{60}^+ ion beam. The ion beam current was 300pA, and the area cleaned was 500×500 µm^2. The Si^+ ion signal was monitored during the sputter cleaning and after 100 seconds of sputtering was found to be no longer decreasing.

After ion beam cleaning, the sample surface was then ion imaged using a Bi_3^+ ion beam in burst alignment mode (BAM) for high lateral resolution. The ion beam current was 0.003pA and the area analysed was 200×200 µm^2 with 512×512 pixels. A total of 20 scans were carried out, and the total ion beam dose was kept well below the static SIMS limit.

2.9 Mass Spectra

Once the ion images had been taken, mass spectra were taken in specific regions of the mineralised nodules. The mass spectra were obtained using the Bi^+ ion beam in high current bunched mode (HCBM) with a beam current of 1pA at 100 µs cycle time for high mass resolution and good ion yields. The analytical area was 50×50 µm^2 with 128×128 pixels. A total of 50 scans were taken and again the ion beam dose was below the static SIMS limit.

2.9 Scanning electron microscopy (SEM) was performed on a JEOL JSM 5610 LV, operated at 20 kV. The SEM images were taken from the same surface area which had been analysed by SIMS.

3. Results

3.1 STEM-EELS

At day 28, the OBs were embedded within mineralized nodules containing a collagenous matrix and mineralized collagen (Figure 1). Mitochondria in the OBs contained dense mineral aggregates with a disordered morphology with a diameter of 47.6±16.8 nm (n=50). The composition and morphology of the granules was characterized by STEM-EELS (Figure 2). EELS spectrum

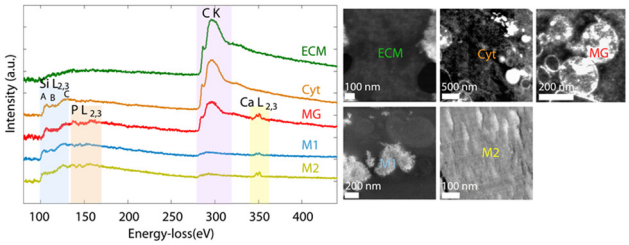

Figure 2: EEL spectra acquired from several regions in OB nodule; mitochondria granule (MG), cytoplasm (Cyt), extracellular matrix (ECM), mineral aggregate (M1) and mineral deposit (M2). The backgrounds were subtracted using a power law model,and aligned and shifted along the y-axis. Each spectrum was labelled with the same colour as the marked area they were obtained from. Si $L_{2,3}$ edge at 99 eV present in all spectra, except the one from ECM. The spectra obtained from MG, M1 and M2 show P $L_{2,3}$ and Ca $L_{2,3}$ edges at 132 and 346 eV, respectively. The C K edge is present in all spectra at 280 eV.

acquired from these mitochondrial granules show a characteristic P $L_{2,3}$- and Ca $L_{2,3}$- edges at 132 and 346 eV, respectively. Further characterization of these mitochondrial granules, including the high resolution TEM images, are described in our previous publication[10]. The distribution and composition of silicon-containing material were studied in several regions of the OB nodules. Si $L_{2,3}$- edges were evident in representative spectra taken from several areas (Figure 2), including the mitochondria (MG), cytoplasm (Cyt), and small and large aggregates of mineral (M1 and M2). The Si $L_{2,3}$ edge had two peaks split by 8 eV (labelled with A and B), and a broad peak (C) which is more intense than the first two peaks. These EEL spectra had a near edge structure which corresponds to tetrahedral SiO_4^{4-} units[22, 23].

3.2 ToF-SIMS

In order to confirm that the silicon detected was not solely due to contamination, the embedded OB nodules were subsequently analysed using ToF-SIMS. To calibrate the instrument, a sample of 0.8 wt% silicon-substituted hydroxyapatite (Si-HA) was used as a standard to identify the Si and Ca peaks. Figure 3 shows the mass spectra obtained with the most relevant Si and Ca peaks indicated. On the standard Si-HA sample the SiO^+ peak is hidden by the very strong $^{44}Ca^+$ peak, and contamination also masks the SiO_2^+ peak. However, the Si^+, $SiCaO^+$, and SiO_4^+ peaks were resolved, with a detection limit for Si^+ of approximately 40ppm. This analysis confirmed that silicon is present as a silicate in synthetic Si-HA.

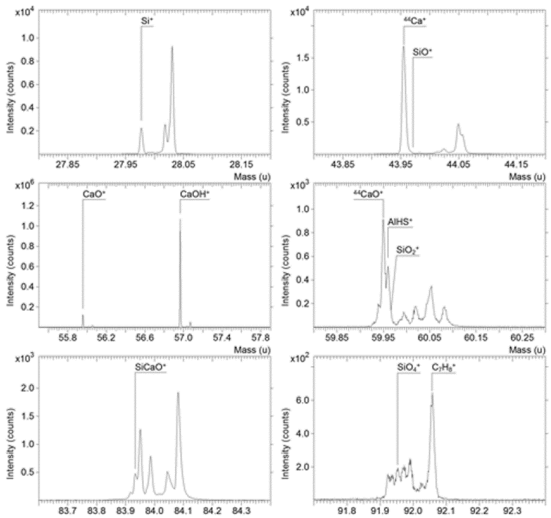

Figure 3: Mass spectra obtained from the Si-HA standard.

Initial ion images obtained from the surface of embedded mineralised nodules, which had been cut by ultramicrotomy for STEM-EELS analysis, indicated the presences of surface contamination as the surface was entirely covered with Si

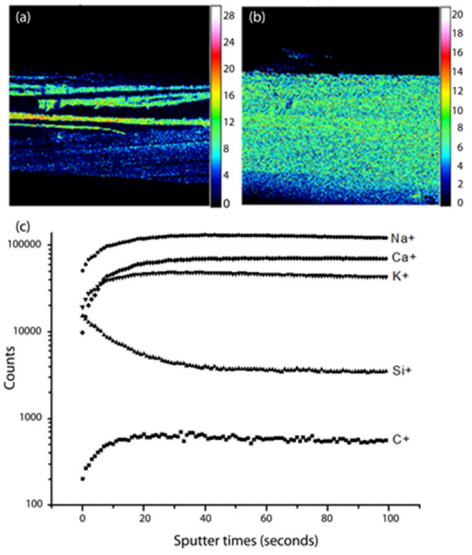

Figure 4: Secondary Ca+ (a) and Si+ (b) images of the OB nodule (500x500 µm2) using Bi_3+ ion beam. c) Depth profiles showing the intensity of C, Na, Si, K, and Ca, ions monitored during surface sputter cleaning using C_{60}^+ ions.

containing compounds (Figure 4b). Ca^+ ion images highlighted the mineralised regions in OB nodules (Figure 4a). The mass spectrumtaken from the surface clearly showed the characteristic peaks of PDMS (main peaks at $SiCH_3^+$, $SiC_2H_7^+$, SiC_3H^+, $Si_2C_5H_{15}O^+$, $Si_3C_5H_{15}O_3^+$ and $Si_3C_7H_{21}O_2^+$)[24] (Supplementary Figure 1). To remove the contamination, the sample was sputter cleaned with a C_{60}^+ sputter gun. During the sputter cleaning C^+, Na^+, Si^+, K^+ and Ca^+ secondary ions were monitored. The depth

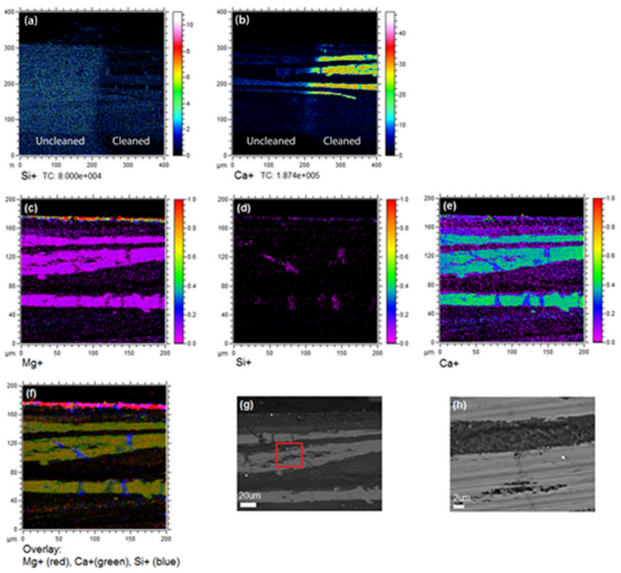

Figure 5: Secondary ion images (a) and (b) show respectively the Si and Ca distributions in the OB nodules from the unclean and cleaned regions. The ion images on the sputter cleaned region show the (c) Mg (d) Si and (e) Ca localization in the OB nodule. A false coloured overlay of these three ion signals is shown in (f). A back scattered image showing the same region as the ion images is shown in (g). The higher magnification back scattered image in (h) of the marked area in (g) shows a crack where silicon localises in mineralised ECM.

profile shows a decrease of Si^+ intensity as the organic contaminant was removed, while C^+, Na^+, K^+ and Ca^+ increased in intensity. The surface was sputter cleaned until all ion intensities became constant (Figure 4c).

Ion images taken after the C_{60}^+ sputtering clearly show the extent of the surface contamination. A large region of the surface was mapped to show both the un-cleaned and sputter cleaned region (Figure 5a, b). Figure 5c, d and e show the Mg^+, Si^+ and Ca^+ ion maps, respectively. The distribution of Mg^+ follows closely the distribution of Ca+ which are the main constituents of the extracellular mineral phase of bone [(1)]. Mass spectra were taken in both the un-cleaned and cleaned regions (Supplementary information Figure 1). The mass spectrum on the un-cleaned part of the surface identified PDMS as the contaminating organic. After the C_{60}^+ sputter clean, most PDMS peaks are no longer visible. Figure 5(b) shows that the organic contaminant clearly suppresses the Ca^+ ion signal, but once removed, the structure of the OB nodule surface can be seen.

A smaller area in the cleaned region was then ion mapped in order to investigate the silicon distribution. Figure 5e shows ion maps of Ca^+ which represent calcified regions in the mineralised nodules. The silicon ion map (Figure 5d) shows the localisation of silicon compounds only in areas that were devoid of any calcium, but not throughout the entire nodule. Backscattered SEM images obtained in the same region as the SIMS ion maps showed cracks in the mineralised regions (Figure 5g and h). The cracks observed in these images correlate to the region rich in silicon in Figure 5d.

3.3 Chemical analysis of the non-contaminated samples

Since,the TOF SIM result suggested that PDMS contamination

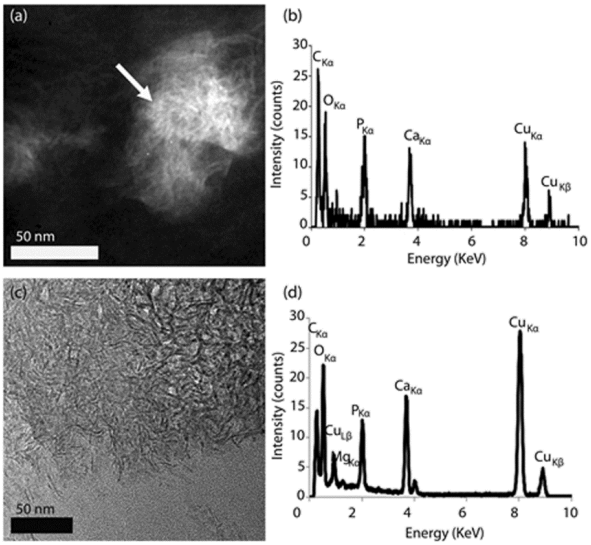

Figure 6: a) STEM HAADF image of a small mineral aggregate (arrow) b) (point) EDX spectrum acquired from the small aggregate in (a) (3s acquisition), the spectrum shows PKα and CaKα peaks. c) Bright field TEM image showing a larger aggregate and d) EDX spectrum taken from mineralised region in (c) with the beam concentrated on the aggregate (100s acquisition), the spectrum shows MgKα and CaKα peaks.

was mainly on the surface of the samples, STEM- EELS and STEM-EDX experiments were conducted on new sample sections (in regions where cracks were absent) which were handled with extra care so as not to generate silicon contamination. In order to remove the surface silicon contamination, a few micrometers of the surface contaminated block was cut away by sectioning with a diamond knife in the ultramicrotome, before collecting sections for analysis. Sections were stored on a filter paper, away from plastic or glass containers which may act as a source of PDMS contamination. EDX analysis did not detect silicon compounds in either the small or large mineral aggregates (Figure 6). EDX spectra instead detected the presence of calcium and a small amount of magnesium (Figure 6d). The collagenous matrix and mineral deposits in the OB nodules were analysed using STEM-EELS to map the silicon distribution again (Figure 7). Silicon was not detected in collagenous matrix (Figure 7a); however, EEL spectra taken from a mineral deposit (Figure 7b) showed a very low intensity signal at the position of Si $L_{2,3}$ -edge (99 eV).

4. Discussion

The main obstacle in mapping the distribution of silicon within biological samples is in first eliminating any silicon-containing contamination. The silicon signal in the EEL spectra generated from contamination also makes accurate detection and quantitative analysis of the P $L_{2,3}$ edge difficult as the Si $L_{2,3}$ edge overlaps with the pre-edge P $L_{2,3}$ background signal. Here, we demonstrated that complementary analysis using STEM-EELS and SIMS enabled analyses of the distribution, coordination environment of silicon in OB nodules and also the detection of surface contamination. The study conclusively showed that the surface of the sample was contaminated with PDMS which can be removed by ensuring that the sample does not come into contact with the plastic TEM grid boxes or petri dishes at any point during sample preparation. When the silicon contaminants were fully removed, silicon was absent from the majority of the nodules, including the OB cytoplasm and collagenous matrix. PDMS contamination may be introduced from exposure to the plastic containers, such as boxes, moulds and bags[24], and even the laboratory atmosphere[25]. This implies that samples can be contaminated during both preparation and post processing. However, our SIMS results showed that PDMS contamination was not in the resin that infiltrated into the sample, but it was only on the surface. After sputter cleaning with a C_{60}^+ ion beam, the OB nodule structure could be clearlyion mapped, however, some Si^+ ions were observed in a crack on the sample surface.

EEL spectroscopy indicated a trace level of Si-species present within the aggregates of calcium phosphate crystals located on the collagen and in the peripheral region of mineralised matrix, possibly the newly mineralised regions of the OB nodules. In the SIMS maps the distribution of Mg^+ follows closely the distribution of Ca^+ which are the main constituents of the extracellular mineral phase of bone[1]. The magnesium may substitute for calcium in the hydroxyapatite lattice, which explains its presence[1]. However, the presence of silicon in mineral aggregates was not verified by EDX

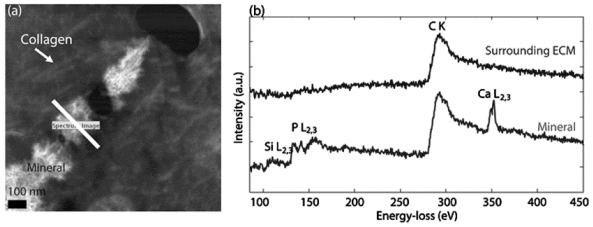

Figure 7: HAADF STEM image taken from partially mineralised collageneous matrix and EELS spectra acquired in those regions (marked areas). EELS spectra were background subtracted using a power law model, aligned and shifted along the y axis. a) The mineral aggregates on the collageneous matrix (arrow indicating collagen fibrils) showing a line scan across the mineral aggregate where EELS spectrum were acquired. b) Spectra taken from the collagen and mineral were summed separately, marked as mineral (red) and ECM (blue), respectively. The sum spectrum taken from the ECM shows the C K edge at 280eV, while the sum spectrum from mineral (red) show P $L_{2,3}$(132eV), C K(280 eV), Ca$L_{2,3}$(346 eV) edges and a very low intensity peak at the position of the Si$L_{2,3}$ edge (99 eV).

analysis. Increased detectability of silicon by EELS aligns with previous reports which have shown increased sensitivity of EELS of silicon compared to EDX for analysis of $L_{2,3}$ shell excitations in the EEL spectrum and the K_α emission line in the X-ray spectrum[26]. To our knowledge this is the first time that spatially resolved EDX and EELS has been used to characterise the distribution of silicon in HPF/FS prepared mineralising tissues.

Previous reports have suggested that silicon localises in active growth areas of young vertebrate bone[1, 4]. Silicon has also been found to co-localise with Ca and O in $CaCO_3$ in the exocuticle of *Ligiaitalica Fabricius* cyanobacteria[27]. The fact that we only detected low levels silicon within the mineralised nodules, even using state-of-the-art analytical detectors and HPF/FS preparation techniques which will preserve the distribution of ions within the

nodules, brings into question whether the silicon detected in previous reports[1,4] arose partially due to contamination or movement and redistribution of ions during tissue processing. Alternatively, the silicon may only sequester in the osteoid tissue at the growth plate and at earlier stages of bone formation, or the silicon present in the un-mineralised collagen was below the detection limit of the instruments used in this work. Our study correlates with other reports which show that primary osteoblasts can form a mineralised matrix without additional silicon-species[16,19,28]. An absence of silicon has been shown to lead to an abnormality of skeleton development in rats and chickens[2,3], however to date, no one has reported on the distribution and composition of Si in OB cultures. Studies have only reported on the positive effects of supplemented silicon on osteoblast activity, collagen arrangement and mineralisation[5-8]. In order to rule out whether silicon would affect mineralisation or alter the ultrastructure of mineralised osteoblasts nodules, further studies need to be carried out which compare the ultrastructure of mineralised osteoblast nodules cultured with, and without, supplemented silicon. Analysis using the new generation of quantum GIF detectors may also make it possible to improve on the detection of silicon within tissues.

Conclusions

STEM-EELS taken from mineral deposits surrounding the OB nodules showed a very low intensity signal at the position of Si $L_{2,3}$ edge (99 eV). In contrast, silicon was not detected by EELS in the collagen matrix. We were not able to detect the presence of silicon convincingly within the mineralised nodules after 28 days culture using EDX or TOF-SIMS, which may raise questions about whether the silicon detected in bone in previous reports[1, 4] arose partially due to contamination or redistribution and movement of ions within the tissue. We suggest that a combination of analytical nanospectroscopy techniques of FS/HPF prepared samples can be applied to further elucidate whether silicon is present in bone in the early stages of collagen mineralisation or in diseased tissues. Moreover, these methods can be used to characterise the coordination environment of the silicon in bone which will provide new insights into the role that silicon plays in mineralisation processes. This correlative analytical approach could also be applied to characterise chemical speciation of ions such as silicon from bioactive ceramics and glasses to elucidate the underlying mechanisms controlling their bioactivity.

Notes and references

[a]*Department of Materials, Imperial College London, London, United Kingdom, Tel. 02075949691, Email: a.porter@imperial.ac.uk*
[b]*National Nanotechnology Center, National Science and Technology Development Agency, Pathum Thani, 12120 Thailand,*
[c]*Department of Craniofacial Development and Stem Cell Biology, King's College London, London SE1 9RT UK, Email:e.gentleman@kcl.ac.uk*
[d]*London Research Institute Lincoln's Inn Fields Laboratories, WC2A 3LY,*
[e]*Department of Materials Science and Engineering, The Ohio State University, Columbus, Ohio 43210 USA, Email:* mccomb.29@osu.edu
[f]*Department of Bioengineering, Imperial College London, London SW7 2AZ UK, Email:m.stevens@imperial.ac.uk*

† Electronic Supplementary Information (ESI) available: [Supplementary figure 1 Full mass spectra for (a) un-cleaned OB nodule and (b) surface of sputter cleaned OB nodule]. See DOI: 10.1039/b000000x/

Acknowledgements

The authors acknowledge to FEI Nanoport for providing the STEM-EDX data. S.B. was supported by a fellowship from the Royal Thai Government. A.P gratefully acknowledges the European research council for an individual investigator grant (Project number 257182). M.M.S thanks the European Research Council for an Individual Investigator Grant (Naturale).

References

1 W. J. Landis, D. D. Lee, J.T. Brenna, S. Chandra and G.H Morrison.. *Calcif Tissue Int*, 1986, **38**, 52-59.
2 K. Schwarz, and D.B. Milne. *Nature*, 1972, **239(5371)**, 333 -334.
3 E. M. Carlisle. *Science*, 1972, **178(4061)**, 619-621.
4 E. M. Carlisle. *Science*, 1970, **167(3916)**, 279-280.
5 P. E. Keeting, M. J. Oursler, K. E. Wiegand, S. K. Bonde, T. C. Spelsberg, B.L. Riggs. *Journal of Bone and Mineral Research*, 1992, **7(11)**, 1281-1289.
6 C. M. Botelho, R. A. Brooks, S. M. Best, M. A. Lopes, J.D. Santos, N. Rushton, W. Bonfield. *Journal of Biomedical Materials Research Part A*, 2006, **79A(3)**, 723-730.
7 E. S. Thian, J. Huang, S.M. Best, Z. H. Barber, R. A. Brooks, N. Rushton, W. Bonfield. *Biomaterials*, 2006, **27(13)**, 2692-2698.
8 A. E. Porter, N. Patel, J. N. Skepper, S. M. Best, W. Bonfield. *Biomaterials*, 2004, **25(16)**, 3303-3314.
9 E. Gentleman, R. J. Swain, N.D. Evans, S. Boonrungsiman, G. Jell, M. D. Ball, T.A. Shean, M.L. Oyen, A. Porter, M. M. Stevens. *Nat Mater*, 2009, 8(9) 763-770.
10 S. Boonrungsiman, E. Gentleman, R, Carzaniga, N.D. Evans, D. W. McComb, A. Porter, M. M. Stevens. *Proceedings of the National Academy of Sciences*, 2012, **28, 109(35)**, 14170-5.
11 T. Buckland, and J, Arcos, Biomedical filler. 2009: U.S.
12 K. A. Hing, B. Annaz, S. Saeed, P. A. Revell, T. Buckland. J *Mater Sci Mater Med*. 2005, **16,** 467–475.
13 L. Malaval, F. Liu, P. Roche, J. E. Aubin. *J Cell Biochem*, 1999, **74(4)**, 616 -27.
14 D. M. Reffitt, N. Ogston, R. Jugdaohsingh, H.F. Cheung, B. A. Evans. R. P. Thompson, J. J. Powell, G. N. Hampson. *Bone*, 2003, **32(2)**, 127-135.
15 B. Zimmermann, H. C. Wachtel, and C. Noppe. *Cell and Tissue Research*, 1991, **263**, 483-493.
16 B. Ecarot-Charrier, N. Shepard, G. Charette, M. Grynpas, F. H. *Bone*, 1988, **9,** 147-154.
17 I. Titorencu, V. Jinga, E. Constantinescu, A. Gafencu, C. Ciohodaru, I. Manolescu, C. Zaharia, M. Simionescu. *Cytotherapy*, 2007, **9(7)**, 682 -696.
18 H. A. Declercq, R. M. Verbeeck, L. I. De Ridder, E. H. Schacht, M. J. Cornelissen. Biomaterials, 2005, **26(24)**, 4964 -4974.
19 U. Bhargava, M. Bar-Lev, C. G. Bellows, J. E. Aubin. *Bone*, 1988, **9**, 155-163.
20 V. Sottile, A. Thomson, and J. McWhir. 2003, **5(2)**, 149-155.
21 L. D. K. Buttery, S. Bourne, J. D. Xynos, H. Wood, F. J. Hughes, S. P. Hughes, V. Episkopou, J. M. Polak. *Tissue Engineering*, 2001, **7(1)**, 89 -99.
22 P. L. Hansen, R. Brydson and D. W. McComb. *Microsc. Microanal. Microstruct.* 1992, **3(2-3)**, 213-219.
23 P. E. Batson,. et al., *Ultramicroscopy*, 1987, **22(1-4)**, 89-101.
24 C. J. Vickerman, D. and Briggs. *UK and Surface Spectra Limited.* 2001, IM publications.
25 G. J. Leggett, J. C. Vickerman, D. Briggs, and M. J. Hearn. *Journal of the Chemical Society, Faraday Transactions*, 1992, **88(3)**, 297-309.
26 R. D. Leapman, J. A. Hung. *Microsc. Microanal. Microstruct.* 1991, **2**, 231-244.
27. N. B. Matsko, I. Letofsky-Papst, M. Dittrich, W. Grogger, J. Strus, F. Hofer. *Journal of Structural Biology*, 2011, **174(1)**, 180-186.
28 C. Barragan-Adjemian, D. Nicolella, W. Dusevich, M. R. Dallas, J. D. Eick, and L.F. Bonewald. *Calcified tissue International*, 2006, **79(5)**, 340-353.